

# Are Cu<sub>2</sub>Te-Based Compounds Excellent Thermoelectric Materials?

Kunpeng Zhao, Ke Liu, Zhongmou Yue, Yancheng Wang, Qingfeng Song, Jian Li, Mengjia Guan, Qing Xu, Pengfei Qiu,\* Hong Zhu, Lidong Chen,\* and Xun Shi\*

Most of the state-of-the-art thermoelectric (TE) materials exhibit high crystal symmetry, multiple valleys near the Fermi level, heavy constituent elements with small electronegativity differences, or complex crystal structure. Typically, such general features have been well observed in those well-known TE materials such as Bi<sub>2</sub>X<sub>3</sub>, SnX-, and PbX-based compounds (X = S, Se, and Te). The performance is usually high in the materials with heavy constituent elements such as Te and Se, but it is low for light constituent elements such as S. However, there is a great abnormality in Cu<sub>2</sub>X-based compounds in which Cu<sub>2</sub>Te has much lower TE figure of merit (*zT*) than Cu<sub>2</sub>S and Cu<sub>2</sub>Se. It is demonstrated that the Cu<sub>2</sub>Te-based compounds are also excellent TE materials if Cu deficiency is sufficiently suppressed. By introducing Ag<sub>2</sub>Te into Cu<sub>2</sub>Te, the carrier concentration is substantially reduced to significantly improve the *zT* with a record-high value of 1.8, 323% improvement over Cu<sub>2</sub>Te and outperforms any other Cu<sub>2</sub>Te-based materials. The single parabolic band model is used to further prove that all Cu<sub>2</sub>X-based compounds are excellent TE materials. Such finding makes Cu<sub>2</sub>X-based compounds the only type of material composed of three sequent main group elements that all possess very high *zT*s above 1.5.

With the increasingly serious environmental pollution and intensified energy crisis, exploitation and utilization of new kinds of clean energy resources are imperative. Among them, thermoelectric (TE) conversion technology based on high-performance TE materials enables direct energy conversion between heat and electricity through the movement of internal phonons and charge carriers.<sup>[1–4]</sup> It has shown extensive and important prospects in power generation using industrial waste heat and electronic refrigeration.<sup>[5]</sup> The energy conversion efficiency of a TE material is mainly determined by its dimensionless figure of merit, defined as  $zT = \sigma S^2 T / (\kappa_L + \kappa_e)$ , where  $\sigma$ ,  $S$ ,  $T$ ,  $\kappa_L$ , and  $\kappa_e$  are the electrical conductivity, Seebeck coefficient, absolute temperature, lattice thermal conductivity, and electronic thermal conductivity, respectively. The general criteria for high *zT*s require high crystal symmetry for materials, many valleys (carrier pockets) near the Fermi

level, heavy elements with small electronegativity differences between the constituent elements, or complex crystal structure, etc.<sup>[6–10]</sup> For the constituent elements in the same group such as S, Se, and Te, the heavy one (Te and Se) always has large atomic mass for low  $\kappa_L$  and more covalent bonding character for large carrier mobility ( $\mu_H$ ) and thus outstanding electrical transports.<sup>[10]</sup> Therefore, the *zT*s are usually high in tellurides and selenides, but they are low in sulfides. This is the general phenomenon that has been observed in those well-known TE materials such as Bi<sub>2</sub>X<sub>3</sub>, SnX-, and PbX-based compounds (X = S, Se, and Te).<sup>[11–47]</sup> As shown in **Figure 1**, the *zT* values gradually improve as the anion element change from S to Se and then to Te. However, the case is different in Cu<sub>2</sub>X-based liquid-like TE materials that are among the hottest materials in recent TE study. They possess exceptionally low thermal conductivity and excellent *zT*s with the values of 1.7–1.9 for Cu<sub>2</sub>S, 1.5–2.3 for Cu<sub>2</sub>Se, and 0.4–1.1 for Cu<sub>2</sub>Te (see **Figure 1**).<sup>[48–62]</sup> It is quite abnormal and interesting that the *zT* in Cu<sub>2</sub>Te is lower than those in Cu<sub>2</sub>S and Cu<sub>2</sub>Se. As we known, tellurium is less electronegative, thus the chemical bonds between Cu and Te should be less ionic as compared with those in Cu<sub>2</sub>S and Cu<sub>2</sub>Se, which is beneficial for large  $\mu_H$  and electrical transports. Besides, the  $\kappa_L$  in Cu<sub>2</sub>Te is expected lower than or similar to those in Cu<sub>2</sub>S and Cu<sub>2</sub>Se because tellurium is much heavier than sulfur and


Dr. K. Zhao, Prof. X. Shi  
State Key Laboratory of Metal Matrix Composites  
School of Materials Science and Engineering  
Shanghai Jiao Tong University  
Shanghai 200240, China  
E-mail: xshi@sjtu.edu.cn

K. Liu, Prof. H. Zhu  
University of Michigan-Shanghai Jiao Tong University Joint Institute  
Shanghai Jiao Tong University  
Shanghai 200240, China

Z. Yue, Y. Wang, Q. Song, J. Li, M. Guan, Q. Xu, Prof. P. Qiu,  
Prof. L. Chen, Prof. X. Shi  
State Key Laboratory of High Performance Ceramics and Superfine  
Microstructure

Shanghai Institute of Ceramics  
Chinese Academy of Sciences  
Shanghai 200050, China  
E-mail: qiupf@mail.sic.ac.cn; cld@mail.sic.ac.cn

Z. Yue, Y. Wang, Q. Song, J. Li, M. Guan, Q. Xu, Prof. L. Chen,  
Prof. X. Shi  
Center of Materials Science and Optoelectronics Engineering  
University of Chinese Academy of Sciences  
Beijing 100049, China

 The ORCID identification number(s) for the author(s) of this article can be found under <https://doi.org/10.1002/adma.201903480>.

DOI: 10.1002/adma.201903480

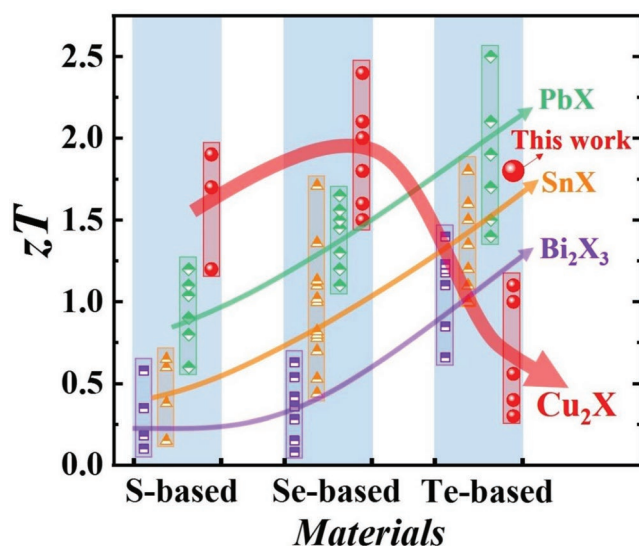


**Figure 1.** Reported  $zT$  values of polycrystalline  $PbX$ -,  $SnX$ -,  $Bi_2X_3$ -, and  $Cu_2X$ -based ( $X = S, Se,$  and  $Te$ ) TE materials. The red sphere symbol represents the data of  $Cu_2Te$  in this study. The other data are taken from refs. [11–62].

selenium. These two features definitely make  $Cu_2Te$  potentially high  $zT$ s superior to  $Cu_2S$  and  $Cu_2Se$ . The deep analysis shows that such abnormality is mainly ascribed to two aspects. On the one hand, the hole concentration ( $p_{H1}$ ) of  $Cu_2Te$  is too high ( $>10^{21} \text{ cm}^{-3}$ ) owing to its severe copper deficiency.<sup>[60]</sup> On the other hand,  $Cu_2Te$  has too complex phase diagram to control material's quality, especially it has at least five phase transitions from its melting point to room temperature.<sup>[63]</sup> Although a few strategies have been used to tune the lattice defects and TE properties of  $Cu_2Te$ , the current maximum  $zT$  is only around 1.1,<sup>[60]</sup> which is much smaller than those in  $Cu_2S$  and  $Cu_2Se$ . This is in contradiction with the general trend observed in other typical TE materials (see Figure 1). Furthermore, this leaves the open questions what is the true  $zT$  in  $Cu_2Te$  and are  $Cu_2Te$ -based compounds excellent TE materials? In this study, we demonstrate that the  $zT$  in  $Cu_2Te$ -based compounds can be as high as 1.8 (Figure 1). Same as  $Cu_2S$  and  $Cu_2Se$ , they are excellent TE materials when their lattice defects and phase transition features are well tuned and optimized.

$Cu_2Te$  has too large hole concentrations ( $p_{H1}$ ) due to the presence of large amount of intrinsic Cu deficiency. Improving Cu amount can lower the Cu deficiency within a certain range but such reduction is very limited. Previous study showed that the vacancy formation energies of  $Ag_2Te$  are gradually decreased after the substitution of Cu at Ag sites.<sup>[64]</sup> As a result, the carrier concentration of  $Ag_{2-x}Cu_xTe$  is gradually increased upon increasing the Cu contents. Since  $Ag_2Te$  has the similar cubic structure as  $Cu_2Te$  at high temperature, we thus expect the carrier concentration of  $Cu_2Te$  can be reduced by alloying Ag at Cu sites. Thus, herein we try to choose Ag to replace Cu to balance the Cu deficiency. The room temperature X-ray diffraction (XRD) patterns measured on powder  $Cu_2Te + x\% Ag_2Te$  ( $x = 0, 15, 35, 40, 50,$  and  $55$ ) are depicted in Figure 2a. The phase compositions of pristine  $Cu_2Te$  are very complicated according to the literatures.<sup>[60]</sup> Our XRD data show that it

consists of multiple phases, including hexagonal, monoclinic, and orthorhombic phases (Figure S1, Supporting Information). After introducing  $Ag_2Te$  into  $Cu_2Te$ , some new diffraction peaks appear in the XRD patterns, which are mainly indexed to the hexagonal  $CuAgTe$  phase. These data show that it is inclined to form secondary phase rather than forming solid-solutions at room temperature for  $Cu_2Te + x\% Ag_2Te$ . Similar phenomenon was also observed in  $Cu_2Se-Ag_2Se$  and  $Cu_2S-Ag_2S$  systems.<sup>[59,65]</sup> However, pure phase is observed after going through the phase transitions at high temperatures. As demonstrated in Figure 2b, nearly all the diffraction peaks at 900 K can be indexed to the  $Cu_2Te$  cubic structure (PDF#053116) with the space group of  $F43m$ . This suggests that all the samples transform into single cubic phase at high temperatures and the second phase at room temperature dissolve into the matrix after the final structural transition. Besides, the diffraction peaks are shifted to a lower angle upon increasing the  $Ag_2Te$  content, indicating that the lattice constants increase with the increase of  $Ag_2Te$  content.

Figure 2c plots the measured differential scanning calorimetry (DSC) curves for  $Cu_2Te + x\% Ag_2Te$  ( $x = 0, 15, 35, 50,$  and  $55$ ). For  $Cu_2Te$ , five successive phase transitions are observed with the transition temperatures somewhat different from the literatures due to its complex phase compositions. The number and temperature of phase transition, and peak intensity of DSC curves are all changed when adding Ag into  $Cu_2Te$ . Specifically, the temperature of the last phase transition between hexagonal phase and cubic phase is weakened and lowered from 815 K in  $Cu_2Te$  to 720 K in  $Cu_2Te + 15\% Ag_2Te$ , and finally disappears in  $Cu_2Te + 55\% Ag_2Te$  (see Figure 2d). This is also consistent with that Ag is dissolved into the  $Cu_2Te$  matrix with increasing the temperature. Such reduced phase transition temperature  $T_c$  is mainly attributed to the decreased ratio of the enthalpy change  $\Delta H$  to the entropy change  $\Delta S$ .

Figure 3 displays the temperature dependence of TE properties for  $Cu_2Te + x\% Ag_2Te$  ( $x = 0, 15, 35, 40, 50,$  and  $55$ ). When  $x$  is less than 50, the electrical conductivity  $\sigma$  decreases in the entire temperature range as the content of  $Ag_2Te$  increases. Specifically, the room temperature  $\sigma$  decreases significantly from  $4.2 \times 10^5 \text{ S m}^{-1}$  for  $Cu_2Te$  to  $1.0 \times 10^5 \text{ S m}^{-1}$  for  $Cu_2Te + 50\% Ag_2Te$ . The reverse trend at around  $x = 55$  may be related to the decreased band gap  $E_g$  since  $CuAgTe$  has a much lower  $E_g$  than that of  $Cu_2Te$ .<sup>[64]</sup> As the temperature increases, the electrical conductivity is roughly decreased except for the phase transition regions, behaving as a highly degenerate semiconductor. In contrast, the Seebeck coefficient  $S$  of  $Cu_2Te + x\% Ag_2Te$  is roughly increased with increasing temperature. At room temperature,  $S$  is scarcely changed or even decreased when the  $Ag_2Te$  content is larger than 15%. The reason for this should be that  $Cu_2Te$  is a p-type semiconductor while  $CuAgTe$  is an n-type semiconductor at room temperature,<sup>[64]</sup> thus the total Seebeck coefficients are partly counterbalanced. However, at high temperatures, all the samples have single cubic phases with one dominant type of carriers, i.e., holes. Therefore, the Seebeck coefficient increases significantly with increasing the  $Ag_2Te$  content. The increased Seebeck coefficient coupled with the decreased electrical conductivity implies that the hole concentration is reduced at high temperatures. We have tried to corroborate our speculation by measuring the carrier concentrations at different temperature. Unfortunately, no reliable data are obtained at high temperature.

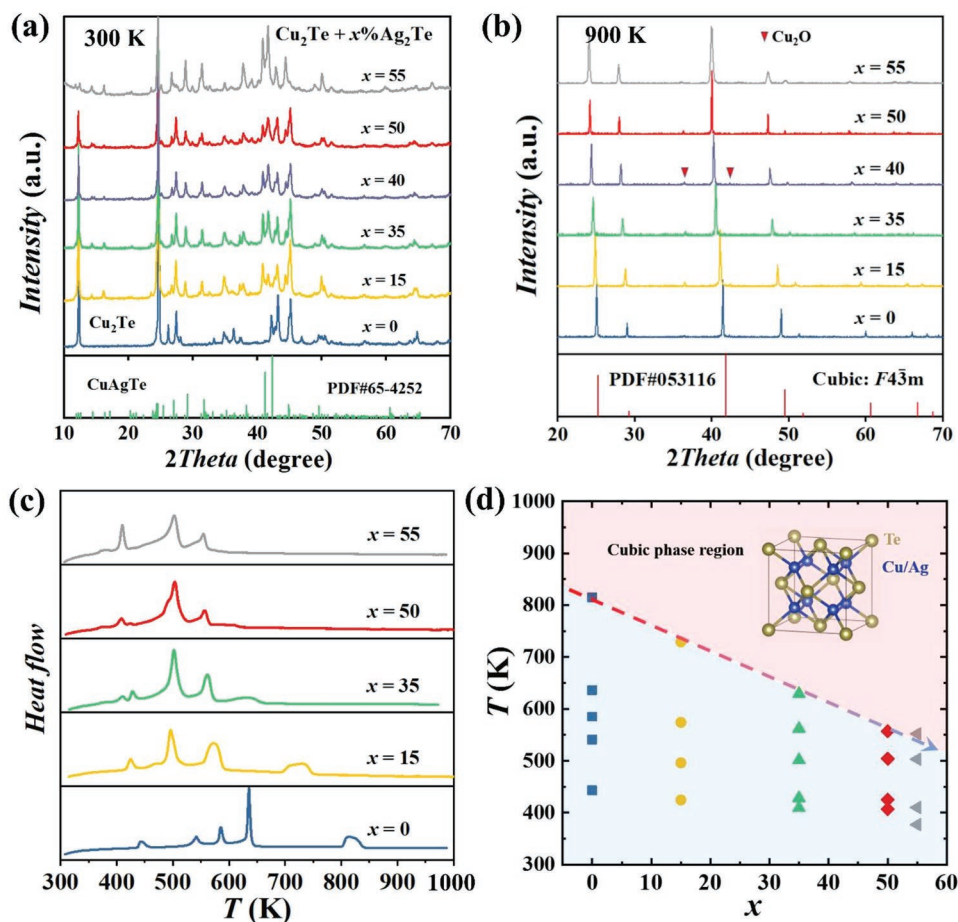


**Figure 2.** PXRD for  $\text{Cu}_2\text{Te} + x\% \text{Ag}_2\text{Te}$  ( $x = 0, 15, 35, 40, 50,$  and  $55$ ) at a)  $300 \text{ K}$  and b)  $900 \text{ K}$ . Some weak reflections belong to  $\text{Cu}_2\text{O}$  are marked with red triangles. The oxidation of  $\text{Cu}_2\text{Te} + x\% \text{Ag}_2\text{Te}$  during the processes of fabrication or measurement should be avoided considering the poor TE performance of  $\text{Cu}_2\text{O}$ .<sup>[66,67]</sup> c) DSC curves measured from  $310$  to  $1000 \text{ K}$ . d) Phase transition temperature  $T_c$  as a function of  $\text{Ag}_2\text{Te}$  content. The inset illustrates the cubic crystal structure of  $\text{Cu}_2\text{Te}$ .

We thus performed defect formation energy ( $E_{\text{form}}$ ) calculations by using the high temperature cubic structures for  $\text{Cu}_2\text{Te}$  and  $\text{CuAgTe}$  (see Figure S3, Supporting Information). The  $E_{\text{form}}$  values for Cu vacancy ( $V_{\text{Cu}}$ ) or/and Ag vacancy ( $V_{\text{Ag}}$ ) are calculated according to the equation

$$E_{\text{form}} = E_{\text{tot}}[\text{defected}] - E_{\text{tot}}[\text{perfect}] + \sum_i n_i \mu_i + qE_f + E_{\text{corr}} \quad (1)$$

where  $E_{\text{tot}}[\text{defected}]$  and  $E_{\text{tot}}[\text{perfect}]$  are the total energy of defected and perfect structures, respectively;  $\sum_i n_i \mu_i$  is the summation over the atomic chemical potentials;  $q$  is the charge of defect;  $E_f$  is the fermi energy; and  $E_{\text{corr}}$  is the correction due to spurious electrostatic interaction of charged cell in periodic boundary calculation. The generalized gradient approximation (GGA) level band gap is zero for  $\text{Cu}_2\text{Te}$  and  $\text{CuAgTe}$ , leading to negligible  $E_{\text{corr}}$ . The atomic chemical potentials were calculated from the ternary phase diagram for Cu-Ag-Te, constructed by using the Pymatgen code based on density functional theory ground state energies from the Materials Project database.<sup>[68,69]</sup> The calculation results based on the  $2 \times 2 \times 2$  supercell are shown in Figure 4. The slanting lines with negative slope represent the defect formation energies for negatively

charged  $V_{\text{Cu}}$  and  $V_{\text{Ag}}$  defects. The Cu vacancy formation energy in  $\text{Cu}_2\text{Te}$  is very low, suggesting that  $V_{\text{Cu}}$  defects are prone to be formed during the fabrication processes. Thus, severe copper precipitation and quite high hole carrier concentration are expected in  $\text{Cu}_2\text{Te}$ , which is consistent with the experiment observation. The carrier concentration of  $\text{Cu}_2\text{Te}$  should be scarcely changed from room temperature to high temperatures although it experiences complex phase transitions. With the addition of Ag, the  $V_{\text{Cu}}$  formation energy is increased within all the Fermi level range, implying that the formation of  $V_{\text{Cu}}$  is suppressed. Besides, we also take into account the possible formation of  $V_{\text{Ag}}$ , whose formation energy is higher than that of Cu vacancy (see Figure 4). This indicates that  $V_{\text{Ag}}$  is more difficult to be created in  $\text{CuAgTe}$  as compared with  $V_{\text{Cu}}$ . Furthermore, the convergence tests of the size effects on defect formation energies have been also performed for  $\text{Cu}_2\text{Te}$  and  $\text{CuAgTe}$ . Three different supercells, i.e.,  $1 \times 1 \times 1$ ,  $2 \times 2 \times 2$ , and  $3 \times 3 \times 3$  were tested. As shown in Figure S4 in the Supporting Information, the calculated energies between the  $2 \times 2 \times 2$  and  $3 \times 3 \times 3$  supercells are very close. The trends for energy variation of Cu vacancy or Ag vacancy in different supercells are also the same. Therefore, the substitution of Ag for Cu can decrease

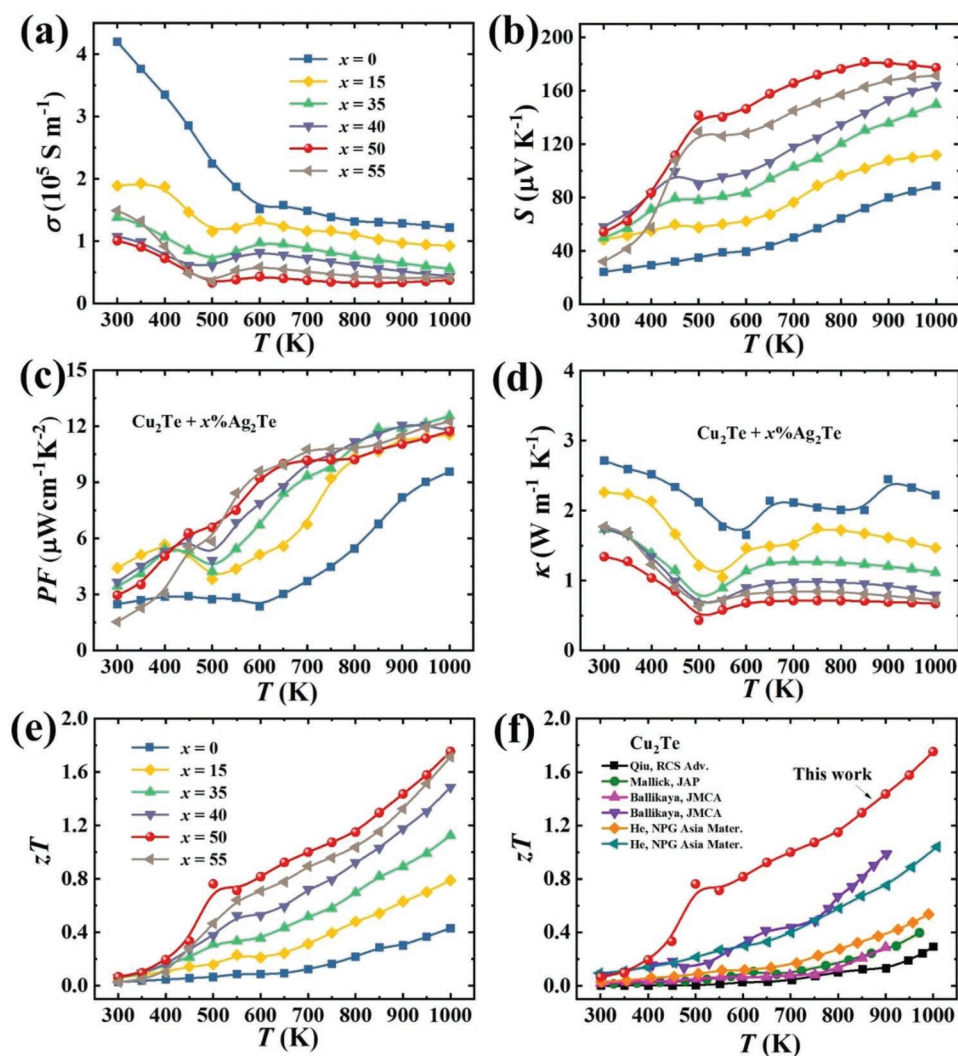


**Figure 3.** Temperature dependence of TE properties for  $\text{Cu}_2\text{Te} + x\% \text{Ag}_2\text{Te}$  ( $x = 0, 15, 35, 40, 50,$  and  $55$ ). a) Electrical conductivity  $\sigma$ , b) Seebeck coefficient  $S$ , c) power factor  $PF$ , d) total thermal conductivity  $\kappa$ , and e) TE figure of merit  $zT$ . f) Comparison of  $zT$  values from 300 to 1000 K for several reported  $\text{Cu}_2\text{Te}$ -based TE materials.<sup>[59–62]</sup>

the formation of cation vacancies, resulting in much lower hole concentrations.

The power factors calculated from the formula  $PFs = S^2\sigma$  are shown in Figure 3c. The PF for pristine  $\text{Cu}_2\text{Te}$  is around  $2.8 \mu\text{W cm}^{-1} \text{K}^{-2}$  below 600 K and subsequently increases with increasing temperature. A maximum PF of  $9.5 \mu\text{W cm}^{-1} \text{K}^{-2}$  is obtained at 1000 K for  $\text{Cu}_2\text{Te}$ . After introducing  $\text{Ag}_2\text{Te}$  into  $\text{Cu}_2\text{Te}$ , the PFs increase in the entire temperature range except for  $\text{Cu}_2\text{Te} + 55\% \text{Ag}_2\text{Te}$ , which shows a low PF near room temperature because of the influence of minor carriers (i.e., electrons). Nevertheless, in the middle temperature range, the PFs are greatly improved due to the suppression of phase transition temperature and the reduction of hole concentration. For instance, a high PF value of  $9 \mu\text{W cm}^{-1} \text{K}^{-2}$  is achieved at 600 K for  $\text{Cu}_2\text{Te} + 50\% \text{Ag}_2\text{Te}$ , which is five times higher than that for pristine  $\text{Cu}_2\text{Te}$  at the same temperature.

Figure 3d displays the total thermal conductivity  $\kappa$  as a function of temperature for  $\text{Cu}_2\text{Te} + x\% \text{Ag}_2\text{Te}$  ( $x = 0, 15, 35, 40, 50,$

and  $55$ ). They show complicated temperature dependencies in the temperature range from 300 to 1000 K due to the existence of multiple phase transitions. The  $\kappa$  is significantly decreased with increasing  $\text{Ag}_2\text{Te}$  content, which is mainly attributed to the decreased contribution of charge carriers to thermal transport. The lattice thermal conductivity  $\kappa_L$  for  $\text{Cu}_2\text{Te} + x\% \text{Ag}_2\text{Te}$  is calculated and shown in Figure S5 in the Supporting Information. All the samples exhibit ultralow lattice thermal conductivity  $\kappa_L$  with the values around  $0.3 \text{ W m}^{-1} \text{K}^{-1}$  at 900 K, which is even lower than the minimum lattice thermal conductivity ( $\kappa_{\text{min}}$ ) estimated by Cahill's model (see the details in the Supporting Information).<sup>[70]</sup>

Figure 3e presents the temperature dependence of  $zT$  for  $\text{Cu}_2\text{Te} + x\% \text{Ag}_2\text{Te}$  ( $x = 0, 15, 35, 40, 50,$  and  $55$ ). At low temperature, both holes and electrons are involved in transport, resulting in relatively low  $zT$  values. However, at high temperature, the TE performance is greatly improved over a large temperature range, which can be traced to the suppressed phase

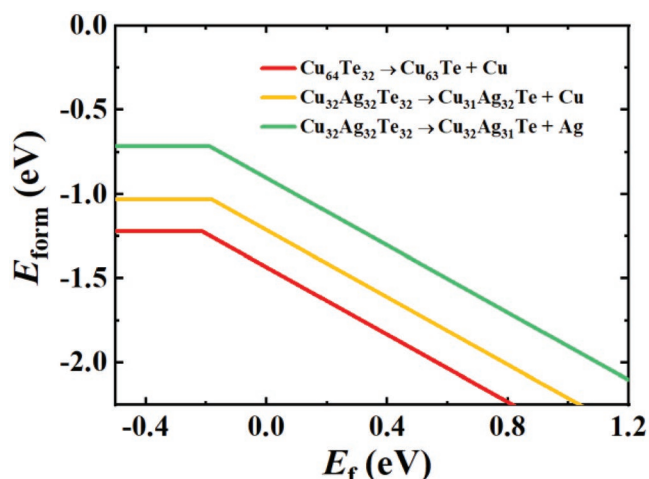


**Figure 4.** Calculated defect formation energy  $E_{\text{form}}$  for copper/silver vacancy in  $\text{Cu}_2\text{Te}$  and  $\text{CuAgTe}$  as a function of Fermi energy. A  $2 \times 2 \times 2$  supercell containing 96 atoms, i.e.,  $\text{Cu}_{64}\text{Te}_{32}$  or  $\text{Cu}_{32}\text{Ag}_{32}\text{Te}_{32}$ , is constructed for calculations. Zero Fermi energy is with respect to the valence band maximum for respective compounds.

transition temperature and the reduced carrier concentration. Specifically, the maximum  $zT$  value for pristine  $\text{Cu}_2\text{Te}$  is only 0.4 and it is remarkably boosted to 1.8 for  $\text{Cu}_2\text{Te} + 50\% \text{Ag}_2\text{Te}$  at 1000 K. This is a 323% improvement over  $\text{Cu}_2\text{Te}$  itself and outperforms any other  $\text{Cu}_2\text{Te}$ -based material reported so far (Figure 3f).<sup>[59–62]</sup>

To further elucidate on the high TE performance of  $\text{Cu}_2\text{Te}$ , we modeled their TE properties using a single parabolic band (SPB) model with the carrier mobility limited by acoustic phonon scattering.<sup>[44,51]</sup> In comparison, the data of  $\text{Cu}_2\text{S}$  and  $\text{Cu}_2\text{Se}$  are also modeled. The experimental data at 900 K are selected because all materials have same cubic structures at this temperature. Thus, the effect of different crystal structures on TE properties can be excluded. The model details are shown in the Supporting Information. Because the Hall data at 900 K is absent, we do not have the exact drift mobility  $\mu_0$  or effective mass  $m^*$ . However, we can fit the  $S$ - $\sigma$  (Seebeck coefficient vs electrical conductivity) curves by taking the weighted mobility ( $\mu_0 m^{*3/2}$ ) as a single parameter (see Equation (S6), Supporting Information). As shown in Figure 5a, the red dashed line is calculated by using a weighted mobility  $\mu_0 m^{*3/2}$  of  $19.6 m_e^{3/2} \text{ cm}^2 \text{ V}^{-1} \text{ s}^{-1}$ . All the experimental  $S$  data for three different types of materials fall around on this derived line. This strongly suggests that  $\text{Cu}_2\text{Te}$ -,  $\text{Cu}_2\text{Se}$ -, and  $\text{Cu}_2\text{S}$ -based compounds have comparable weighted mobility parameter  $\mu_0 m^{*3/2}$  at high temperature. Thus,  $\text{Cu}_2\text{Te}$ -,  $\text{Cu}_2\text{Se}$ -, and  $\text{Cu}_2\text{S}$ -based compounds may have similar good electrical transport properties, which is further supported by the calculated power factors (see Figure 5b). All the data for  $\text{Cu}_2\text{S}$ ,  $\text{Cu}_2\text{Se}$ , and  $\text{Cu}_2\text{Te}$  show a very nice agreement with the calculated curve. The only difference among  $\text{Cu}_2\text{S}$ ,  $\text{Cu}_2\text{Se}$ , and  $\text{Cu}_2\text{Te}$  is the position of Fermi level. It is near the top of valence band for  $\text{Cu}_2\text{S}$ , in the deep covalent band for  $\text{Cu}_2\text{Te}$ , and in the middle for  $\text{Cu}_2\text{Se}$ . Thus, the electrical conductivity is low in  $\text{Cu}_2\text{S}$ , in the middle in  $\text{Cu}_2\text{Se}$ , and very high in  $\text{Cu}_2\text{Te}$ . According to Figure 5b,

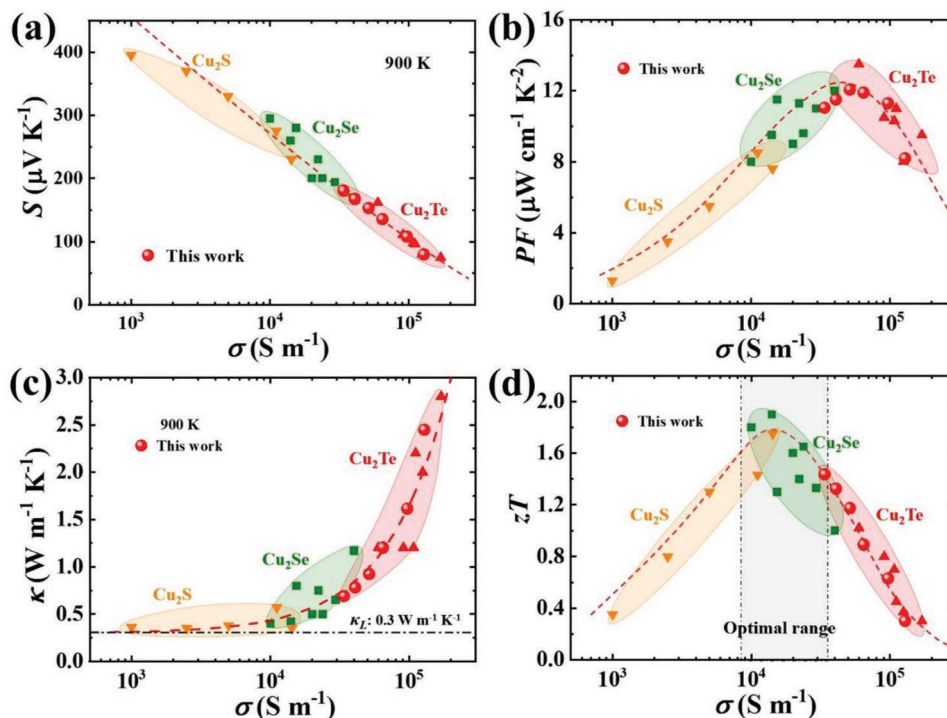


**Figure 5.** Comparison of TE properties among  $\text{Cu}_2\text{Te}$ ,  $\text{Cu}_2\text{Se}$ , and  $\text{Cu}_2\text{S}$ -based materials at 900 K. a) Seebeck coefficient  $S$ , b) power factor  $PF$ , c) total thermal conductivity  $\kappa$ , and d)  $zT$  values as a function of electrical conductivity  $\sigma$ . The red circle symbols are experimental data in this work. The other symbols are the data from refs. [48–62]. The dashed lines are derived from the single parabolic band (SPB) model with the weighted mobility  $\mu_0 m^{*3/2}$  of  $19.6 m_e^{3/2} \text{ cm}^2 \text{ V}^{-1} \text{ s}^{-1}$ .

the optimal electrical conductivity  $\sigma_{\text{opt}}$  for maximized PF is around  $5 \times 10^4 \text{ S m}^{-1}$ , which can be easily achieved in  $\text{Cu}_2\text{Se}$ . Due to the severe copper deficiency,  $\text{Cu}_2\text{Te}$ -based compounds have quite high electrical conductivity ( $\approx 10^5 \text{ S m}^{-1}$ ) that greatly exceeds the  $\sigma_{\text{opt}}$  value. Thus, its PF is relatively low. On the contrary,  $\text{Cu}_2\text{S}$ -based compound has very low electrical conductivity ( $\approx 10^3 \text{ S m}^{-1}$ ) that is much less than the  $\sigma_{\text{opt}}$  value, thus its PF is also very low. The electrical conductivity for  $\text{Cu}_2\text{Se}$ -based compound lies between that of  $\text{Cu}_2\text{Te}$  and  $\text{Cu}_2\text{S}$ . Nevertheless, according to our analysis, the PFs for all the  $\text{Cu}_2\text{X}$  compounds can be tuned to the optimal range when their electrical conductivity and carrier concentration are optimized.

The  $\kappa$ - $\sigma$  (total thermal conductivity vs electrical conductivity) relation is calculated under the assumption that  $\kappa_{\text{l}}$  is  $0.3 \text{ W m}^{-1} \text{ K}^{-1}$  for all materials. This is an acceptable assumption for these liquid-like materials with ultralow lattice thermal conductivity. As plotted in Figure 5c, the experimental data agree well with the calculated curve, indicating that the total thermal conductivity is dominated by carrier thermal conductivity in  $\text{Cu}_2\text{X}$ -based compounds. When increasing electrical conductivity, the total thermal conductivity is greatly improved. Thus,  $\text{Cu}_2\text{S}$ -based compounds generally have very low  $\kappa$ , whereas  $\text{Cu}_2\text{Te}$ -based compounds have quite high  $\kappa$ .

The  $zT$  value as a function of  $\sigma$  is then calculated based on the PF and  $\kappa$  derived above, which is plotted in Figure 5d. The optimal electrical conductivity range for the maximized  $zT$  is around  $(1\text{--}3) \times 10^4 \text{ S m}^{-1}$ , which is slightly lower than that for PF because of the contribution from electronic thermal conductivity. Apparently, the electrical conductivity for  $\text{Cu}_2\text{Se}$  is close to the optimal value, thus high  $zT$ 's are easily achieved in  $\text{Cu}_2\text{Se}$ . Whereas the  $\sigma$  values in  $\text{Cu}_2\text{S}$  and  $\text{Cu}_2\text{Te}$  are either less or larger than the optimal value, resulting in low  $zT$  values. Increasing the  $\sigma$  in  $\text{Cu}_2\text{S}$  and decreasing the  $\sigma$  in  $\text{Cu}_2\text{Te}$  can approach the optimal range for high  $zT$ 's. In this study, when adding Ag into  $\text{Cu}_2\text{Te}$ , the  $\sigma$  is greatly reduced and its TE performance is significantly improved. The above data and analysis clearly demonstrate that  $\text{Cu}_2\text{Te}$  is also an excellent TE material. It is not against the general trend shown in Figure 1. Furthermore, due to the ultralow  $\kappa_{\text{l}}$  in these liquid-like materials, all  $\text{Cu}_2\text{S}$ ,  $\text{Cu}_2\text{Se}$ , and  $\text{Cu}_2\text{Te}$  possess very high  $zT$ 's when their electrical properties are optimized. This is beyond the other TE materials. Currently, it is the only material system that possesses very high  $zT$ 's above 1.5 in the materials with all three constituent elements in the same group such as S, Se, and Te.

While  $\text{Cu}_2\text{X}$ -based liquid-like compounds are promising TE materials with high  $zT$  values, the migration of Cu ions causes long-term stability problems under electric field and/or temperature gradient.<sup>[71–74]</sup> Such stability issue has been well studied recently, which is determined by the critical voltage of Cu ions.<sup>[73]</sup> Even Cu/Ag moves fast, the liquid-like materials can still be stable if the critical voltage is large enough.<sup>[73,74]</sup> The critical voltage for  $\text{Cu}_2\text{X}$ -based materials is around 0.1 V, which is a few orders of higher than the voltage (0.0001 V) used for TE property measurements. To validate the sample stability under small voltage/current, repeatability measurements are performed on  $\text{Cu}_2\text{Te} + 35\% \text{ Ag}_2\text{Te}$  for six cycles with different cycling temperatures. As presented in Figure S6 in the Supporting Information, both the  $\sigma$  and  $S$  show quite good

reproducibility up to 1000 K with just a little change below the phase transition temperatures (<500 K) because of the presence of mixed phases.

To sum up, by introducing  $\text{Ag}_2\text{Te}$  into  $\text{Cu}_2\text{Te}$ , the high carrier concentration in pristine  $\text{Cu}_2\text{Te}$  is substantially reduced to an optimal range, resulting in much reduced thermal conductivity and enhanced power factors over the entire temperature range. Furthermore, the temperature of last phase transition is significantly lowered when increasing Ag content, which benefits to maintain the good TE properties of cubic phase at low temperatures. A maximum  $zT$  of 1.8 is achieved at 1000 K in  $\text{Cu}_2\text{Te} + 50\% \text{ Ag}_2\text{Te}$ , which is the highest reported value for  $\text{Cu}_2\text{Te}$ -based TE materials. An effective SPB model was used to model the transport properties of  $\text{Cu}_2\text{S}$ -,  $\text{Cu}_2\text{Se}$ -, and  $\text{Cu}_2\text{Te}$ -based compounds and it was found that they are all outstanding TE materials. This conclusion is beyond the general trend observed in other TE materials in which very high  $zT$ 's cannot be achieved in all the sulfides, selenides, and tellurides.

## Experimental Section

**Synthesis:** A series of samples with nominal compositions of  $\text{Cu}_2\text{Te} + x\% \text{ Ag}_2\text{Te}$  ( $x = 0, 15, 35, 40, 50, \text{ and } 55$ ) was synthesized by vacuum melting combined with the spark plasma sintering (SPS) process. High purity Cu (Sigma Aldrich, 99.999%), Ag (Sigma Aldrich, 99.999%), and Te (Sigma Aldrich, 99.999%) were weighed out and loaded into boron nitride crucibles that were sealed in a fused silica tube under vacuum. The loaded tubes were slowly heated to 1403 K in 12 h and soaked at this temperature for 6–12 h, then rapidly quenched to room temperature in water. Next, the sealed tubes were heated to 973 K in 8 h, dwelled at this temperature for 6 days, and subsequently cooled to room temperature by turning off the furnace power. The obtained ingots were hand-ground into fine powders using a mortar and a pestle. Then the powders were loaded into a graphite die with a diameter of 10 mm and then consolidated via SPS (Sumitomo SPS-2040) at 773–873 K under a pressure of 50–60 MPa for 5 min. Electrically insulating but thermally conducting boron nitride layers were coated on the carbon foils and the inner sides of the graphite die before the SPS process. Highly dense (>98% of theoretical density) disk-shaped pellets with dimensions of 10 mm in diameter and about 5 mm in thickness were obtained.

**Characterization:** Room-temperature powder X-ray diffraction (RT-PXRD) analysis was performed on Rigaku Rint 2000 with a  $\text{Cu-K}\alpha$  source. High-temperature PXRD patterns were collected at 900 K on a powder X-ray diffractometer (Bruker D8 Advance) with high temperature accessory operating at 45 kV and 200 mA. The sample compositions were measured by field emission scanning electron microscopy (Magellan-400) equipped with energy dispersive X-ray analysis (Horiba 250). The sound speed data were obtained by an ultrasonic measurement system UMS-100 with shear wave transducers of 5 MHz and longitudinal wave transducers of 10 MHz. DSC measurement was carried out using a Netzsch DSC 404FE instrument. The electrical conductivity ( $\sigma$ ) and Seebeck coefficient ( $S$ ) were measured simultaneously in a helium atmosphere using a commercial apparatus (ULVAC ZEM-3). Thermal diffusivity ( $D$ ) was measured via the laser flash method using a Netzsch LFA-457. The pellet density ( $d$ ) was measured by the Archimedes method. The  $C_p$  for  $\text{Cu}_2\text{Te} + 55\% \text{ Ag}_2\text{Te}$  sample was measured by using the commercial DSC equipment (see Figure S7, Supporting Information). The total thermal conductivity was calculated via the equation  $\kappa = d \times C_p \times D$ . The measurement errors for the electrical conductivity, the Seebeck coefficient, and the thermal conductivity were 5%, 7%, and 5%, respectively.

**Defect Formation Energy Calculation:** The present calculations were performed using the Perdew–Burke–Ernzerhof-GGA<sup>[75,76]</sup> with projector-augmented wave method,<sup>[77]</sup> as implemented in the Vienna Ab Initio

Simulation Package (VASP).<sup>[78]</sup> The high temperature cubic structures for Cu<sub>2</sub>Te and CuAgTe with ordered Cu and Ag distribution were adopted for all the calculations (see Figure S3, Supporting Information). Besides, a special quasi-random structure for CuAgTe to mimic a random distribution of Cu and Ag was also adopted based on “mcsqs” code of the Alloy Theoretic Automated Toolkit (ATAT).<sup>[79]</sup> The obtained defect formation energy in the special quasi-random structure was close to that in the ordered structure (see Figure S8, Supporting Information). For simplicity, only the 8c sites were taken into account since the 32f site occupation would make the Cu<sub>2</sub>Te/CuAgTe less stable at 0 K. Three different crystal cells, i.e., 1 × 1 × 1, 2 × 2 × 2, and 3 × 3 × 3 supercells with 6 × 6 × 6, 3 × 3 × 3, and 2 × 2 × 2 gamma centered k-point meshes, respectively, were employed for numerical integrations over the Brillouin zone. A fixed constant occupancy of the defects state was used in calculations. The cutoff energy of the plane wave was set at 520 eV. The energy convergence criterion was chosen to be 5.0 × 10<sup>-3</sup> eV per unit cell. It should be noted that the calculated energy in this study might have large uncertainties (such as the negative formation energies), but the relative value was quoteworthy and the conclusions were reasonable.

## Supporting Information

Supporting Information is available from the Wiley Online Library or from the author.

## Acknowledgements

The authors thank Prof. Yiyang Sun of Shanghai Institute of Ceramics for helpful discussions. This work was financially supported by the National Key Research and Development Program of China (2018YFB0703600), National Natural Science Foundation of China (nos. 51625205 and 51961135106), Key Research Program of Chinese Academy of Sciences (grant no. KFZD-SW-421). P.Q. thanks for the support by the Youth Innovation Promotion Association of CAS under grant no. 2016232.

## Conflict of Interest

The authors declare no conflict of interest.

## Keywords

electrical transport, single parabolic bands, telluride, thermal conductivity, thermoelectric materials

Received: May 31, 2019  
Revised: September 13, 2019  
Published online: October 16, 2019

- [1] X. Shi, L. Chen, C. Uher, *Int. Mater. Rev.* **2016**, *61*, 379.
- [2] W. G. Zeier, A. Zevalkink, Z. M. Gibbs, G. Hautier, M. G. Kanatzidis, G. J. Snyder, *Angew. Chem., Int. Ed.* **2016**, *55*, 6826.
- [3] G. Tan, L. D. Zhao, M. G. Kanatzidis, *Chem. Rev.* **2016**, *116*, 12123.
- [4] T. Zhu, Y. Liu, C. Fu, J. P. Heremans, J. G. Snyder, X. Zhao, *Adv. Mater.* **2017**, *29*, 1605884.
- [5] X. Shi, L. Chen, *Nat. Mater.* **2016**, *15*, 691.
- [6] Y. Pei, X. Shi, A. LaLonde, H. Wang, L. Chen, G. J. Snyder, *Nature* **2011**, *473*, 66.
- [7] J. Zhang, R. Liu, N. Cheng, Y. Zhang, J. Yang, C. Uher, X. Shi, L. Chen, W. Zhang, *Adv. Mater.* **2014**, *26*, 3848.

- [8] J. Li, X. Zhang, Z. Chen, S. Lin, W. Li, J. Shen, I. T. Witting, A. Faghaninia, Y. Chen, A. Jain, *Joule* **2018**, *2*, 976.
- [9] G. J. Snyder, E. S. Toberer, *Nat. Mater.* **2008**, *7*, 105.
- [10] G. A. Slack, in *Handbook of Thermoelectrics* (Ed: D. Rowe), CRC, Boca Raton, FL **1995**, pp. 407–440.
- [11] W. Liu, K. C. Lukas, K. McEnaney, S. Lee, Q. Zhang, C. P. Opeil, G. Chen, Z. Ren, *Energy Environ. Sci.* **2013**, *6*, 552.
- [12] Z. H. Ge, P. Qin, D. He, X. Chong, D. Feng, Y. H. Ji, J. Feng, J. He, *ACS Appl. Mater. Interfaces* **2017**, *9*, 4828.
- [13] Y. Kawamoto, H. Iwasaki, *J. Electron. Mater.* **2014**, *43*, 1475.
- [14] G. L. Sun, L. L. Li, X. Y. Qin, D. Li, T. H. Zou, H. X. Xin, B. J. Ren, J. Zhang, Y. Y. Li, X. J. Li, *Appl. Phys. Lett.* **2015**, *106*, 053102.
- [15] G. Sun, X. Qin, D. Li, J. Zhang, B. Ren, T. Zou, H. Xin, S. B. Paschen, X. Yan, *J. Alloys Compd.* **2015**, *639*, 9.
- [16] F. Hao, P. Qiu, Y. Tang, S. Bai, T. Xing, H.-S. Chu, Q. Zhang, P. Lu, T. Zhang, D. Ren, J. Chen, X. Shi, L. Chen, *Energy Environ. Sci.* **2016**, *9*, 3120.
- [17] B. Poudel, Q. Hao, Y. Ma, Y. Lan, A. Minnich, B. Yu, X. Yan, D. Wang, A. Muto, D. Vashaee, *Science* **2008**, *320*, 634.
- [18] Y. Pan, Y. Qiu, I. Witting, L. Zhang, C. Fu, J.-W. Li, Y. Huang, F.-H. Sun, J. He, G. J. Snyder, C. Felser, J.-F. Li, *Energy Environ. Sci.* **2019**, *12*, 624.
- [19] B. Xu, T. Feng, M. T. Agne, L. Zhou, X. Ruan, G. J. Snyder, Y. Wu, *Angew. Chem., Int. Ed.* **2017**, *56*, 3546.
- [20] Y. Pan, U. Aydemir, J. A. Grovogui, I. T. Witting, R. Hanus, Y. Xu, J. Wu, C. F. Wu, F. H. Sun, H. L. Zhuang, *Adv. Mater.* **2018**, *30*, 1802016.
- [21] B. Zhou, S. Li, W. Li, J. Li, X. Zhang, S. Lin, Z. Chen, Y. Pei, *ACS Appl. Mater. Interfaces* **2017**, *9*, 34033.
- [22] Q. Tan, L.-D. Zhao, J.-F. Li, C.-F. Wu, T.-R. Wei, Z.-B. Xing, M. G. Kanatzidis, *J. Mater. Chem. A* **2014**, *2*, 17302.
- [23] Z.-G. Chen, X. Shi, L.-D. Zhao, J. Zou, *Prog. Mater. Sci.* **2018**, *97*, 283.
- [24] Y. Li, X. Shi, D. Ren, J. Chen, L. Chen, *Energies* **2015**, *8*, 6275.
- [25] Q. Zhang, E. K. Chere, J. Sun, F. Cao, K. Dahal, S. Chen, G. Chen, Z. Ren, *Adv. Energy Mater.* **2015**, *5*, 1500360.
- [26] Y. Luo, J. Yang, Q. Jiang, W. Li, D. Zhang, Z. Zhou, Y. Cheng, Y. Ren, X. He, *Adv. Energy Mater.* **2016**, *6*, 1600007.
- [27] Y. K. Lee, K. Ahn, J. Cha, C. Zhou, H. S. Kim, G. Choi, S. I. Chae, J. H. Park, Y. Lee, C. H. Park, S. P. Cho, S. H. Park, Y. E. Sung, W. B. Lee, T. Hyeon, I. Chung, *J. Am. Chem. Soc.* **2017**, *139*, 10887.
- [28] X. Shi, K. Zheng, M. Hong, W. Liu, R. Moshwan, Y. Wang, X. Qu, Z. G. Chen, J. Zou, *Chem. Sci.* **2018**, *9*, 7376.
- [29] Y. Zhu, J. Carrete, Q.-L. Meng, Z. Huang, N. Mingo, P. Jiang, X. Bao, *J. Mater. Chem. A* **2018**, *6*, 7959.
- [30] G. Tang, W. Wei, J. Zhang, Y. Li, X. Wang, G. Xu, C. Chang, Z. Wang, Y. Du, L. D. Zhao, *J. Am. Chem. Soc.* **2016**, *138*, 13647.
- [31] R. Moshwan, L. Yang, J. Zou, Z.-G. Chen, *Adv. Funct. Mater.* **2017**, *27*, 1703278.
- [32] Q. Zhang, B. Liao, Y. Lan, K. Lukas, W. Liu, K. Esfarjani, C. Opeil, D. Broido, G. Chen, Z. Ren, *Proc. Natl. Acad. Sci. USA* **2013**, *110*, 13261.
- [33] G. Tan, L. D. Zhao, F. Shi, J. W. Doak, S. H. Lo, H. Sun, C. Wolverton, V. P. Dravid, C. Uher, M. G. Kanatzidis, *J. Am. Chem. Soc.* **2014**, *136*, 7006.
- [34] R. Al Rahal Al Orabi, N. A. Mecholsky, J. Hwang, W. Kim, J.-S. Rhyee, D. Wee, M. Fornari, *Chem. Mater.* **2016**, *28*, 376.
- [35] J. Tang, B. Gao, S. Lin, J. Li, Z. Chen, F. Xiong, W. Li, Y. Chen, Y. Pei, *Adv. Funct. Mater.* **2018**, *28*, 1803586.
- [36] S. Johnsen, J. He, J. Androurakis, V. P. Dravid, I. Todorov, D. Y. Chung, M. G. Kanatzidis, *J. Am. Chem. Soc.* **2011**, *133*, 3460.
- [37] L.-D. Zhao, J. He, C.-I. Wu, T. P. Hogan, X. Zhou, C. Uher, V. P. Dravid, M. G. Kanatzidis, *J. Am. Chem. Soc.* **2012**, *134*, 7902.
- [38] Y. Zheng, S. Wang, W. Liu, Z. Yin, H. Li, X. Tang, C. Uher, *J. Phys. D: Appl. Phys.* **2014**, *47*, 115303.

- [39] J. Androulakis, I. Todorov, J. He, D.-Y. Chung, V. Dravid, M. Kanatzidis, *J. Am. Chem. Soc.* **2011**, *133*, 10920.
- [40] Q. Zhang, H. Wang, W. Liu, H. Wang, B. Yu, Q. Zhang, Z. Tian, G. Ni, S. Lee, K. Esfarjani, G. Chen, Z. Ren, *Energy Environ. Sci.* **2012**, *5*, 5246.
- [41] Z. Chen, B. Ge, W. Li, S. Lin, J. Shen, Y. Chang, R. Hanus, G. J. Snyder, Y. Pei, *Nat. Commun.* **2017**, *8*, 13828.
- [42] L. You, Y. Liu, X. Li, P. Nan, B. Ge, Y. Jiang, P. Luo, S. Pan, Y. Pei, W. Zhang, G. J. Snyder, J. Yang, J. Zhang, J. Luo, *Energy Environ. Sci.* **2018**, *11*, 1848.
- [43] Z. Chen, Z. Jian, W. Li, Y. Chang, B. Ge, R. Hanus, J. Yang, Y. Chen, M. Huang, G. J. Snyder, Y. Pei, *Adv. Mater.* **2017**, *29*, 1606768.
- [44] Y. Pei, A. D. LaLonde, N. A. Heinz, X. Shi, S. Iwanaga, H. Wang, L. Chen, G. J. Snyder, *Adv. Mater.* **2011**, *23*, 5674.
- [45] P. Jood, M. Ohta, A. Yamamoto, M. G. Kanatzidis, *Joule* **2018**, *2*, 1339.
- [46] X. Su, S. Hao, T. P. Bailey, S. Wang, I. Hadar, G. Tan, T.-B. Song, Q. Zhang, C. Uher, C. Wolverton, X. Tang, M. G. Kanatzidis, *Adv. Energy Mater.* **2018**, *8*, 1800659.
- [47] H. J. Wu, L. D. Zhao, F. S. Zheng, D. Wu, Y. L. Pei, X. Tong, M. G. Kanatzidis, J. Q. He, *Nat. Commun.* **2014**, *5*, 5515.
- [48] Y. He, T. Day, T. Zhang, H. Liu, X. Shi, L. Chen, G. J. Snyder, *Adv. Mater.* **2014**, *26*, 3974.
- [49] L. Zhao, X. Wang, F. Y. Fei, J. Wang, Z. Cheng, S. Dou, J. Wang, G. J. Snyder, *J. Mater. Chem. A* **2015**, *3*, 9432.
- [50] H. Liu, X. Shi, F. Xu, L. Zhang, W. Zhang, L. Chen, Q. Li, C. Uher, T. Day, G. J. Snyder, *Nat. Mater.* **2012**, *11*, 422.
- [51] K. Zhao, A. B. Blichfeld, H. Chen, Q. Song, T. Zhang, C. Zhu, D. Ren, R. Hanus, P. Qiu, B. B. Iversen, F. Xu, G. J. Snyder, X. Shi, L. Chen, *Chem. Mater.* **2017**, *29*, 6367.
- [52] B. Yu, W. Liu, S. Chen, H. Wang, H. Wang, G. Chen, Z. Ren, *Nano Energy* **2012**, *1*, 472.
- [53] X. Su, F. Fu, Y. Yan, G. Zheng, T. Liang, Q. Zhang, X. Cheng, D. Yang, H. Chi, X. Tang, Q. Zhang, C. Uher, *Nat. Commun.* **2014**, *5*, 4908.
- [54] K. Zhao, A. B. Blichfeld, E. Eikeland, P. Qiu, D. Ren, B. B. Iversen, X. Shi, L. Chen, *J. Mater. Chem. A* **2017**, *5*, 18148.
- [55] L. L. Zhao, X. L. Wang, J. Y. Wang, Z. X. Cheng, S. X. Dou, J. Wang, L. Q. Liu, *Sci. Rep.* **2015**, *5*, 7671.
- [56] R. Nunna, P. Qiu, M. Yin, H. Chen, R. Hanus, Q. Song, T. Zhang, M.-Y. Chou, M. T. Agne, J. He, G. J. Snyder, X. Shi, L. Chen, *Energy Environ. Sci.* **2017**, *10*, 1928.
- [57] A. A. Olvera, N. A. Moroz, P. Sahoo, P. Ren, T. P. Bailey, A. A. Page, C. Uher, P. F. P. Poudeu, *Energy Environ. Sci.* **2017**, *10*, 1668.
- [58] K. Zhao, H. Duan, N. Raghavendra, P. Qiu, Y. Zeng, W. Zhang, J. Yang, X. Shi, L. Chen, *Adv. Mater.* **2017**, *29*, 1701148.
- [59] S. Ballikaya, H. Chi, J. R. Salvador, C. Uher, *J. Mater. Chem. A* **2013**, *1*, 12478.
- [60] Y. He, T. Zhang, X. Shi, S.-H. Wei, L. Chen, *NPG Asia Mater.* **2015**, *7*, e210.
- [61] M. M. Mallick, S. Vitta, *J. Appl. Phys.* **2017**, *122*, 024903.
- [62] Y. Qiu, J. Ye, Y. Liu, X. Yang, *RSC Adv.* **2017**, *7*, 22558.
- [63] Y. G. Asadov, L. V. Rustamova, G. B. Gasimov, K. M. Jafarov, A. G. Babajev, *Phase Transitions* **1992**, *38*, 247.
- [64] R. Wu, Z. Li, Y. Li, L. You, P. Luo, J. Yang, J. Luo, *J. Materiomics* **2019**, *5*, 489.
- [65] R. Graf, *J. Electrochem. Soc.* **1968**, *115*, 433.
- [66] J. Linnner, A. J. Karttunen, *Phys. Rev. B* **2017**, *96*, 014304.
- [67] A. Young, C. Schwartz, *J. Phys. Chem. Solids* **1969**, *30*, 249.
- [68] S. P. Ong, W. D. Richards, A. Jain, G. Hautier, M. Kocher, S. Cholia, D. Gunter, V. L. Chevrier, K. A. Persson, G. Ceder, *Comput. Mater. Sci.* **2013**, *68*, 314.
- [69] A. Jain, S. P. Ong, G. Hautier, W. Chen, W. D. Richards, S. Dacek, S. Cholia, D. Gunter, D. Skinner, G. Ceder, K. A. Persson, *APL Mater.* **2013**, *1*, 011002.
- [70] D. Cahill, S. Watson, R. Pohl, *Phys. Rev. B* **1992**, *46*, 6131.
- [71] G. Dennler, R. Chmielowski, S. Jacob, F. Capet, P. Roussel, S. Zastrow, K. Nielsch, I. Opahle, G. K. H. Madsen, *Adv. Energy Mater.* **2014**, *4*, 1301581.
- [72] D. R. Brown, T. Day, T. Caillat, G. J. Snyder, *J. Electron. Mater.* **2013**, *42*, 2014.
- [73] P. Qiu, M. T. Agne, Y. Liu, Y. Zhu, H. Chen, T. Mao, J. Yang, W. Zhang, S. M. Haile, W. G. Zeier, J. Janek, C. Uher, X. Shi, L. Chen, G. J. Snyder, *Nat. Commun.* **2018**, *9*, 2910.
- [74] P. Qiu, T. Mao, Z. Huang, X. Xia, J. Liao, M. T. Agne, M. Gu, Q. Zhang, D. Ren, S. Bai, X. Shi, G. J. Snyder, L. Chen, *Joule* **2019**, *3*, 1538.
- [75] J. P. Perdew, K. Burke, *Phys. Rev. Lett.* **1997**, *78*, 1396.
- [76] J. P. Perdew, K. Burke, *Phys. Rev. Lett.* **1996**, *77*, 3865.
- [77] P. E. Blöchl, *Phys. Rev. B* **1994**, *50*, 17953.
- [78] G. Kresse, J. Furthmüller, *Phys. Rev. B* **1996**, *54*, 11169.
- [79] A. van de Walle, P. Tiwary, M. de Jong, D. L. Olmsted, M. Asta, A. Dick, D. Shin, Y. Wang, L.-Q. Chen, Z.-K. Liu, *Calphad* **2013**, *42*, 13.